

ELLERMAN BOMBS AT HIGH RESOLUTION: II. TRIGGERING, VISIBILITY, AND EFFECT ON UPPER ATMOSPHERE

GREGAL J. M. VISSERS, LUC H. M. ROUPPE VAN DER VOORT, AND ROBERT J. RUTTEN

Institute of Theoretical Astrophysics, University of Oslo, P.O. Box 1029 Blindern, N-0315 Oslo, Norway; g.j.m.vissers@astro.uio.no

Draft version October 2, 2018

ABSTRACT

We use high-resolution imaging spectroscopy with the Swedish 1-m Solar Telescope (SST) to study the transient brightenings of the wings of the Balmer H α line in emerging active regions that are called Ellerman bombs. Simultaneous sampling of Ca II 8542 Å with the SST confirms that most Ellerman bombs occur also in the wings of this line, but with markedly different morphology. Simultaneous images from the Solar Dynamics Observatory (SDO) show that Ellerman bombs are also detectable in the photospheric 1700 Å continuum, again with differing morphology. They are also observable in 1600 Å SDO images, but with much contamination from C IV emission in transition-region features. Simultaneous SST spectropolarimetry in Fe I 6301 Å shows that Ellerman bombs occur at sites of strong-field magnetic flux cancellation between small bipolar strong-field patches that rapidly move together over the solar surface. Simultaneous SDO images in He II 304 Å, Fe IX 171 Å, and Fe XIV 211 Å show no clear effect of the Ellerman bombs on the overlying transition region and corona. These results strengthen our earlier suggestion, based on H α morphology alone, that the Ellerman bomb phenomenon is a purely photospheric reconnection phenomenon.

Subject headings: Sun: activity – Sun: atmosphere – Sun: magnetic topology

1. INTRODUCTION

Ellerman bombs are transient brightenings of the outer wings of the Balmer H α line at 6563 Å that occur in solar active regions with much flux emergence (Ellerman 1917). The fairly extended literature on this topic was summarized by Georgoulis et al. (2002) and reviewed more recently by Rutten et al. (2013).

Ellerman bombs are of particular interest because they seem to pinpoint emerging magnetic field. Various topologies have been proposed: reconnection between emerging flux and existing fields (Watanabe et al. 2008; Hashimoto et al. 2010; Morita et al. 2010), reconnection between shearing unipolar fields (Georgoulis et al. 2002; Watanabe et al. 2008; Hashimoto et al. 2010), and a much-elaborated scenario of reconnection between opposite walls of U-shaped fields in undulatory (“sea serpent”) flux emergence (Pariat et al. 2004; Pariat et al. 2006; Watanabe et al. 2008; Pariat et al. 2012a; Pariat et al. 2012b) which started with the Flare Genesis Experiment (Bernasconi et al. 2002; Georgoulis et al. 2002; Schmieder et al. 2004). The concept of undulatory field emergence with reconnection in the low atmosphere has also been studied numerically by Nozawa et al. (1992), Yokoyama & Shibata (1995), Litvinenko (1999), Isobe et al. (2007), Cheung et al. (2008), and Archontis & Hood (2009).

In this paper we study Ellerman bombs using new imaging spectroscopy with the the Swedish 1-m Solar Telescope (SST; Scharmer et al. 2003a). Its field of view and the typical sequence duration permitted by atmospheric seeing in ground-based observing make such data less suited to study Ellerman bomb occurrence as indicator of large-scale active region emergence patterning, but the unprecedented spatial, temporal, and spectral resolution of SST data permits microscopic study of the structure and dynamics of individual Ellerman bombs

with much higher data quality than all earlier studies. This paper is a sequel to Watanabe et al. (2011, henceforth Paper I) who established from such SST data that Ellerman bombs appear as small, rapidly varying, upright “flames” of bright emission in the H α wings that are rooted in magnetic concentrations. These authors concluded that the Ellerman bombs constitute a purely photospheric phenomenon and are hidden at H α line center by overlying chromospheric fibrils. This morphology suggested heating from strong-field magnetic reconnection taking place in the low photosphere, not in the chromosphere as thought so far.

In this sequel we analyze two new SST H α data sets, one with simultaneous Ca II 8542 Å imaging spectroscopy, the other with simultaneous Fe I 6301 Å imaging polarimetry. We also add comparison with ultraviolet imaging in the 1600 Å, 1700 Å, 304 Å, 171 Å, and 211 Å passbands of the Atmospheric Imaging Assembly (AIA; Lemen et al. 2012) on the Solar Dynamics Observatory (SDO). We use these data to broaden the evidence that Ellerman bombs mark strong-field reconnection, to compare Ellerman bomb morphology at high resolution in H α and Ca II 8542 Å, to discuss how to best detect H α Ellerman bombs in ultraviolet AIA images so that the huge AIA database may become available for Ellerman bomb pattern research, and to test claims that Ellerman bombs are related to upper-atmosphere phenomena such as surges and micro-flares.

Our combined H α and Fe I 6301 Å imaging spectroscopy may be regarded as higher-resolution analysis of the type as the Hinode analysis by Matsumoto et al. (2008b), while our comparison of H α and Ca II 8542 Å imaging spectroscopy follows on similar but lower-resolution comparisons by Socas-Navarro et al. (2006), Fang et al. (2006), and Pariat et al. (2007a). There are

many reports on Ellerman bomb appearance in 1600 Å TRACE (Qiu et al. 2000; Georgoulis et al. 2002; Fang et al. 2006; Socas-Navarro et al. 2006; Pariat et al. 2007a; Pariat et al. 2007b; Matsumoto et al. 2008b; Berlicki et al. 2010; Herlender & Berlicki 2011), but none yet on comparison with AIA’s 1700 Å imaging which seems a better Ellerman bomb diagnostic than its 1600 Å imaging.

Finally, there are reports of upper atmosphere response to underlying Ellerman bombs in the form of H α surges (Roy 1973; Roy & Leparskas 1973; Shibata et al. 1982; Matsumoto et al. 2008a; Guglielmino et al. 2010; Paper I) but the ubiquity of such correspondence seems questionable (Paper I). The same holds for correspondence between Ellerman bombs and energetic upper-atmosphere phenomena (Shimizu et al. 2002; Madjarska et al. 2009) of which the ubiquity was also questioned by Schmieder et al. (2004) who found only one Flare Genesis example amidst hundreds of Ellerman bombs. The availability of better-quality short-wavelength imaging with SDO warrants and enables further investigation of such correspondences.

The structure of the paper is as follows. In Sect. 2 we describe the observational procedures and the data. The analysis methods are explained in Sect. 3. The results are presented in Sect. 4 and discussed in Sect. 5. We end the paper with conclusions in Sect. 6.

2. OBSERVATIONS AND DATA REDUCTION

2.1. SST/CRISP data acquisition and reduction

Observational setup—As in Paper I, we use data obtained with the CRisp Imaging Spectropolarimeter (CRISP; Scharmer et al. 2008) at the SST. CRISP and the SST together yield imaging spectropolarimetry at unsurpassed high spatial, spectral and temporal resolution. The telescope is equipped with a real-time tip-tilt and adaptive-optics wave-front correction system (Scharmer et al. 2003b). CRISP is a dual Fabry-Pérot interferometer (FPI) operating in the red part of the spectrum that allows wavelength tuning within 50 ms. The light from the telescope is first guided through an optical chopper which ensures strict synchronization of exposures by three cameras. The wavelength band is selected with a prefilter mounted on a filterwheel that allows a spectral band change within 250–600 ms. CRISP contains two liquid crystals for polarimetry and high-resolution and low-resolution etalons for wavelength selection and tuning. The polarimetric modulation is accomplished by cycling the liquid crystal variable retarders through four different states. An orthogonally polarizing beam splitter behind the FPI divides the light onto two cameras in order to reduce seeing-induced cross-talk (cf. Lites 1987). Between the prefilter and CRISP a few percent of the light is branched off to a camera imaging this wide band to serve as “multi-object” anchor in the post-processing. The three CCD cameras are identical high-speed low-noise Sarnov CAM1M100 cameras with 1K \times 1K chips. They run at 35 fps frame rate with an exposure time of 17 ms.

Data acquisition and reduction—Two SST/CRISP data sets are used in this study. The first was acquired on 2010 June 28 during 08:16–09:06 UT covering 54'' \times 53''

of active region NOAA 11084 containing a sunspot located at $(X, Y) = (-720, -343)$ in standard heliocentric solar coordinates (in arcsec, with the Y -direction positive northward and the X -direction positive westward from the center of the apparent solar disk). Both the H α and Ca II 8542 Å profiles were finely sampled in this observation. Full Stokes data were intended to be taken in the Fe I 6301 Å line at -48 mÅ but unfortunately, the wavelength setting was incorrect; these data are not used in this study.

The second data set was obtained on 2011 May 7 during 08:56–09:52 UT, with the field of view centered on $(X, Y) = (317, 306)$, covering 55'' \times 55'' and containing part of a sunspot and some pores in active region NOAA 11204. In this observation, H α was sampled only at $\Delta\lambda = \pm 1$ Å and at line center. The profiles of Ca II 8542 Å and Fe I 6301 Å were finely sampled including full Stokes polarimetry but we do not use the Ca II data in this study. Further detail including viewing angles, spectral passbands, wavelength samplings, cadences, and durations for both data sets are given in Table 1.

At each H α and Ca II 8542 Å wavelength sampling a “multi-frame” burst of eight exposures was taken. For Fe I 6301 Å in the second data set four exposures were recorded for each liquid-crystal state at each wavelength position. The image scale is 0''.0592 px $^{-1}$, well below the SST’s Rayleigh diffraction limit for H α (0''.17), Ca II 8542 Å (0''.21), and Fe I 6301 Å (0''.16).

Post-processing with Multi-Object Multi-Frame Blind Deconvolution (MOMFBD, van Noort et al. 2005) reduced the remaining high-order image deterioration from atmospheric seeing considerably. In this technique, all images at each tuning position within a line profile scan are tessellated into 64 \times 64 px 2 overlapping subfields that are each MOMFBD-restored independently and then re-assembled. The wide-band images act both as multi-object channel for numerical wavefront sensing and as alignment anchor for the narrow-band CRISP images.

Remaining small-scale seeing deformations due to the non-simultaneity of the sequentially tuned narrowband CRISP images are minimized by application of the cross-correlation method of Henriques (2012). The data are subsequently also corrected for the transmission profile of the prefilter following de la Cruz Rodríguez (2012).

The final post-processing of the image sequences includes correction for the time-dependent image rotation that results from the alt-azimuth configuration of the SST, and destretching following Shine et al. (1994) which removes remaining rubber-sheet distortions. The latter are determined from the wide-band images and then applied to the co-aligned narrow-band ones.

The polarimetric Fe I 6301 Å data were processed following Watanabe et al. (2012), which is a modification of the method developed by Schnerr et al. (2011).

2.2. SDO/AIA data reduction and co-alignment

For both SST data sets we selected overlapping SDO/AIA images in the 1600 Å, 1700 Å, 304 Å, 171 Å, and 211 Å wavelength channels, covering 84'' \times 84'' and centered on the field of view of the SST. The level-1 AIA data were improved to level-1.5 with the SolarSoft `aia_prep.pro` procedure, yielding data with spatial

TABLE 1
OVERVIEW OF THE CRISP DATA SETS ANALYZED IN THIS STUDY.

Data set	Target	Date	Location (μ)	Diagnostic	Prefilter passband [\AA]	CRISP FWHM [m \AA]	Range [\AA]	Sampling [m \AA]	Cadence [s]	Duration [min]
1	AR 11084	2010 Jun 28	0.53	H α 6563 \AA	4.9	66	± 1.9	85	22.4	51
				Ca II 8542 \AA	9.3	111	± 1	55		
2	AR 11204	2011 May 7	0.89	H α 6563 \AA	4.9	66	± 1	1000	27.4	56
				Fe I 6301 \AA	4.6	64	$-0.6-1.7$	48 ^a		

^a The indicated spacing holds between -480 and $+576$ m \AA but two extra continuum samplings were added at -610 m \AA and $+1734$ m \AA .

sampling of $0''.6 \text{ px}^{-1}$, a temporal cadence of 24 s for the 1600 \AA and 1700 \AA data, and 12 s for the other channels. The SST images were co-aligned to the AIA images using bright points in the blue wing of H α and in the 1700 \AA images as reference for cross-correlation, taking the SDO image closest in time per SST image. Figure 1 shows image samples from data set 1; Figure 2 shows image samples from data set 2.

3. ANALYSIS METHODS

3.1. Ellerman bomb detection and selection

In Paper I Ellerman bombs were identified manually on the basis of their flame-like morphology. In this paper we developed an automated detection algorithm through extensive trials in which visual inspection showed which constraints work best to properly recover the Ellerman bomb flames seen in our data. The algorithm consists of four constraints:

1. *Brightness.* A double intensity threshold is applied to the SST H α and Ca II 8542 \AA data. First, only pixels exceeding a threshold of 155% of the average intensity over the whole field of view are passed. Second, a lower threshold of 140% of the average then passes only those pixels that are adjacent to already selected ones.
2. *Size.* To emulate the visually observed flame morphology, we require that at least five of the selected pixels are spatially connected, corresponding to $0''.2-0''.3$ extent.
3. *Continuity.* Detections meeting the above constraints in subsequent images often overlap spatially and are then considered to represent the same event. However, sometimes temporal gaps occur due to variable seeing. We therefore allow that detections may skip up to two frames (~ 50 s) before overlapping again to still be counted as a single event. Also, splitting or merging events are resolved at this stage by propagating the detection with the largest spatial overlap between frames, while the one with the smallest overlap is considered to originate, respectively disappear, at that particular time step.
4. *Lifetime.* Finally, all detections that are visible for less than two consecutive images (corresponding to ~ 45 s and ~ 55 s for data set 1 and 2, respectively) are removed from the sample. Note that this duration threshold differs considerably from the value

of 240 s used in Paper I. It results from trade-off between maximizing the number of detected Ellerman bombs and reducing the number of false identifications.

Summed H α wing data (obtained by taking the average of H α $\pm(0.9-1.1)$ \AA and H α ± 1.1 \AA for data set 1 and 2, respectively), as well as Ca II 8542 \AA summed blue and red wing images (obtained by taking the average of three wing positions covering $\pm(0.6-0.7)$ \AA in either wing separately) were run through this detection algorithm. The selected Ca II wing positions were chosen as such to minimize the effects of overlying fibril obscuration. For comparison purposes, the algorithm was also tested with a single $5\text{-}\sigma$ above average brightness threshold on the 1700 \AA data. Table 2 gives an overview of the detection results after steps 2, 3, and 4 (with the corresponding number of remaining detections in the third through fifth columns, respectively).

TABLE 2
NUMBER STATISTICS FROM AUTOMATED DETECTION.

Set	Diagnostic	Number of detections after threshold		
		Int. & size	Continuity	Lifetime
1	H α 6563 \AA	783	106	78
	Ca II 8542 \AA total ^a	—	—	13
	– Ca II 8542 \AA blue	174	18	9
	– Ca II 8542 \AA red	137	14	13
	Cont. 1700 \AA	294	29	25
2	H α 6563 \AA	436	81	61
	Cont. 1700 \AA	420	37	32

^a Result of combining the detections in both wings of the line and considering spatially overlapping detections at a particular time step to represent the same event.

It should be noted that the number of actual Ellerman bombs is probably higher than suggested by the last column in this table, as a number of detections displays substructure, also sequentially in time, that is not differentiated into separate detections by the algorithm.

Our comparisons between the results of our algorithm tests and the visual appearance of the Ellerman bomb flames in our data was largely done by extensive use of the CRisp SPectral EXplorer of (CRISPEX; Vissers & Rouppe van der Voort 2012) of which the browsing and analysis functionality allows fast confirmation of algorithmic Ellerman bomb detections as well as simultaneous multi-diagnostic comparisons of multiple Ellerman

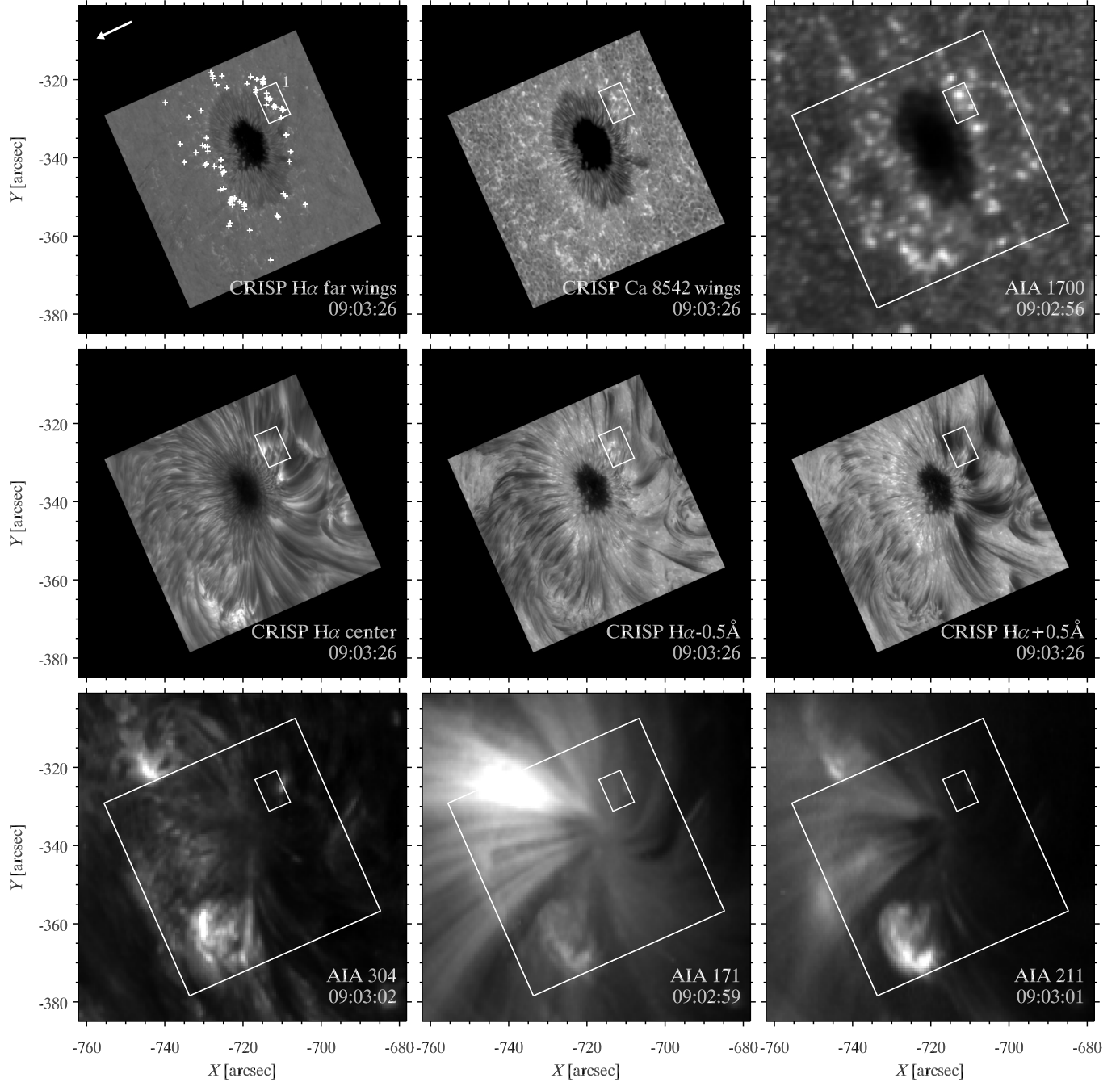


FIG. 1.— Near-simultaneous co-aligned CRISP and AIA image samples from data set 1. The SST field of view is rotated to heliocentric (X, Y) coordinates and is specified by a large white square in the AIA panels. In the first panel the arrow specifies the direction towards the limb and the plus signs specify the locations of all Ellerman bombs detected in data set 1. Each image is scaled independently. The small rectangle marks cutout region-of-interest 1, containing a bright Ellerman bomb at this time which is also seen in the second and third panels. *First row:* photospheric diagnostics $H\alpha$ summed wing ($\pm(0.9-1.1) \text{ \AA}$) intensity, Ca II 8542 \AA summed wing intensity ($\pm(0.6-0.7 \text{ \AA})$), 1700 \AA intensity. *Second row:* chromospheric diagnostics $H\alpha$ line center intensity, $H\alpha$ blue and red wing intensities at $\Delta\lambda = \pm 0.5 \text{ \AA}$. *Third row:* transition region diagnostics 304 \AA , 171 \AA and 211 \AA intensities.

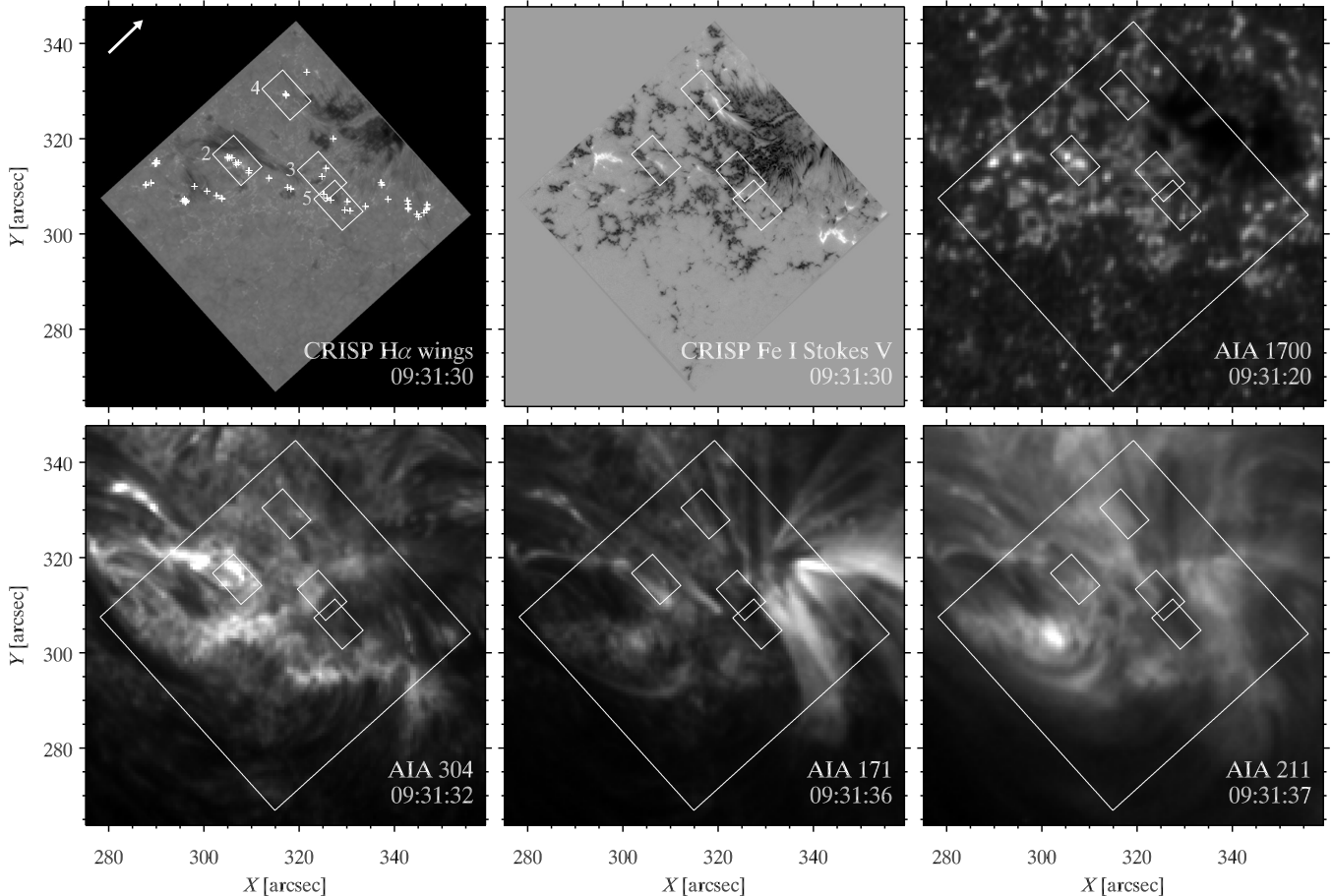


FIG. 2.— Near-simultaneous co-aligned CRISP and AIA image samples from data set 2 in the format of Fig. 1. The small rectangles mark the cutouts of regions of interest 2–5. *Upper row*: photospheric diagnostics $H\alpha$ summed wing intensity ($\pm 1 \text{ \AA}$), Fe 16301 \AA Stokes- V/I , 1700 \AA intensity. *Lower row*: transition region diagnostics 304 \AA , 171 \AA and 211 \AA intensities.

bomb signatures.

3.2. Spectropolarimetric analysis

We investigated the Ellerman bomb behavior in our data with respect to the magnetic field distribution over the surface both qualitatively and quantitatively by comparing summed $H\alpha$ wing and Fe 16301 \AA Stokes- V/I intensity images with the goal to establish a connection between the Ellerman bomb phenomenon and the underlying magnetic and flow fields. Firstly, we determined the distance to the nearest opposite polarity in the Stokes- V/I image at -48 m\AA from line center for every pixel at every time step. Secondly, we derived the photospheric surface flow field from the Fe 16301 \AA continuum images at $+1734 \text{ m\AA}$ using the local correlation tracking technique of Yi & Molowny-Horas (1995), applying a temporal window of 4 minutes and Gaussian spatial smoothing with a halfwidth of $0''.7$.

4. RESULTS

Detection statistics— When applied to the $H\alpha$ data, our algorithm detects 78 and 61 Ellerman bombs in the first and second data set, respectively. Although the longest detections in data set 1 and 2 last about 35 min and 20 min, the detection lifetimes are on average 3.5–4 min and at least 75% of the detections has a lifetime shorter

than 5 min. For the 1700 \AA continuum the lifetimes are longer on average, but the lifetime of the longest living detections is similar to those observed in $H\alpha$, with at least 70% of the detections having a lifetime of 5 min or shorter.

The average area covered by single detections in the $H\alpha$ images is $0.2\text{--}0.3 \text{ arcsec}^2$ and more than 90% has an area smaller than 0.6 arcsec^2 . The detection sizes in the AIA data are larger, with an average of approximately $1.1\text{--}1.3 \text{ arcsec}^2$.

For Ca II 8542 \AA the number of detections is too small to give meaningful statistics, but the results would suggest they have a similar tendency as the 1700 \AA detections, i.e., longer lifetimes and larger area than in $H\alpha$ (although the values are much closer to those of $H\alpha$ than to those of 1700 \AA).

Signature in $H\alpha$ and Ca II 8542 \AA — Figure 3 shows the time evolution in both $H\alpha$ and Ca II 8542 \AA of a few selected Ellerman bombs in data set 1. Detection contours based on both spectral diagnostics are overlaid on the images.

The $H\alpha$ panels (first and third columns) illustrate the basic Ellerman bomb morphology reported in Paper I, i.e., they appear as slender features, upright in the general direction of the limb. This is also shown by the azure $H\alpha$ -based detection contours. However, they are

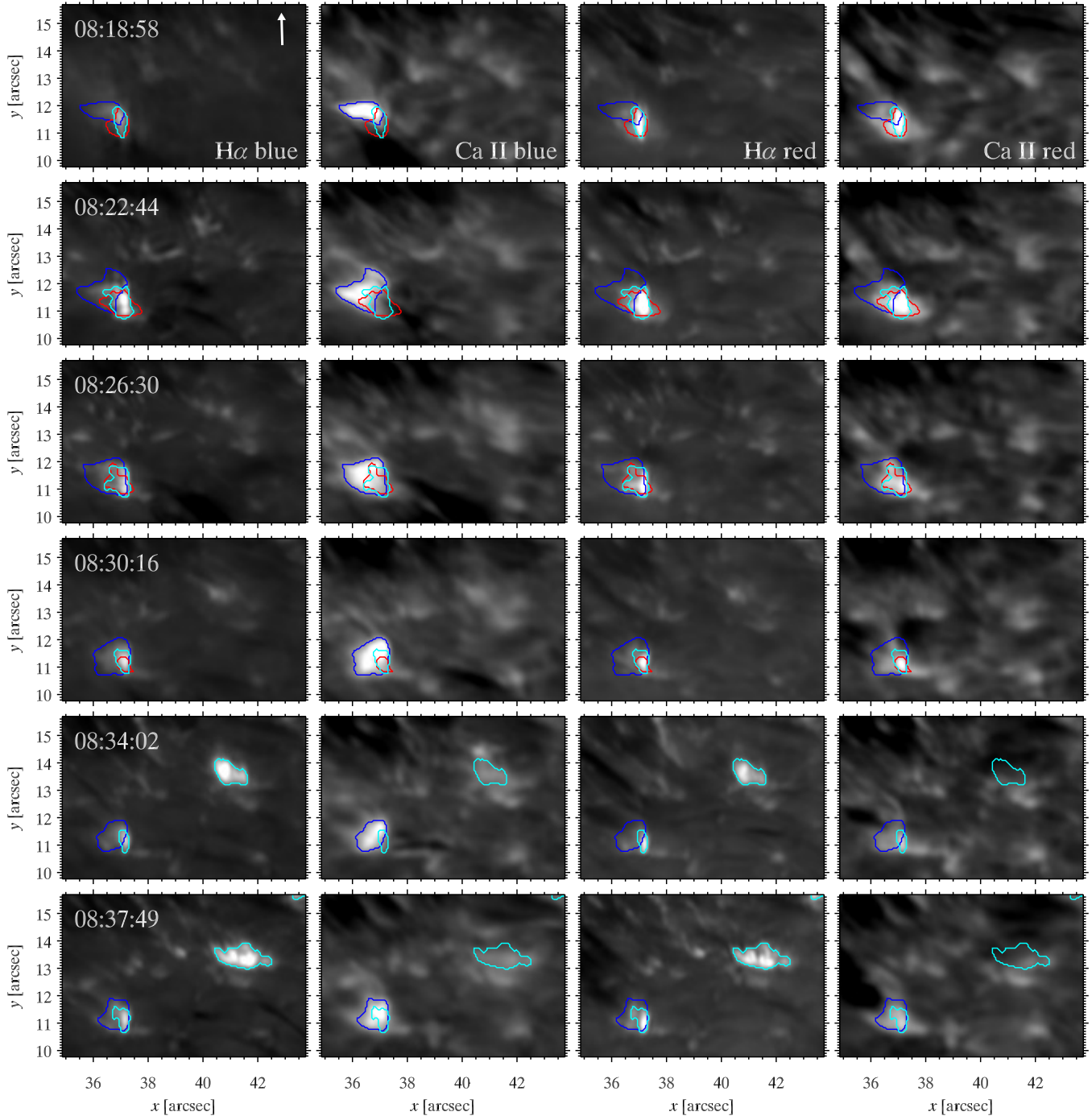


FIG. 3.— Ellerman bomb evolution in a sequence of cutouts in H α blue wing (*first column*), Ca II 8542 Å blue wing (*second column*), H α red wing (*third column*), and Ca II 8542 Å red wing (*fourth column*) for region-of-interest 1 on the center-side of the sunspot in data set 1 (cf. Fig. 1). The cutouts are rotated clockwise by 114° from their orientation in Fig. 2 in order to obtain a close to vertical limbward direction which is indicated by the white arrow in the top left panel. The time in UT is specified in the upper-left corners of the panels in the first column. In all panels the detection contours based on H α (*azure*) and Ca II blue and red wing (*blue* and *red*, respectively) have been overlaid.

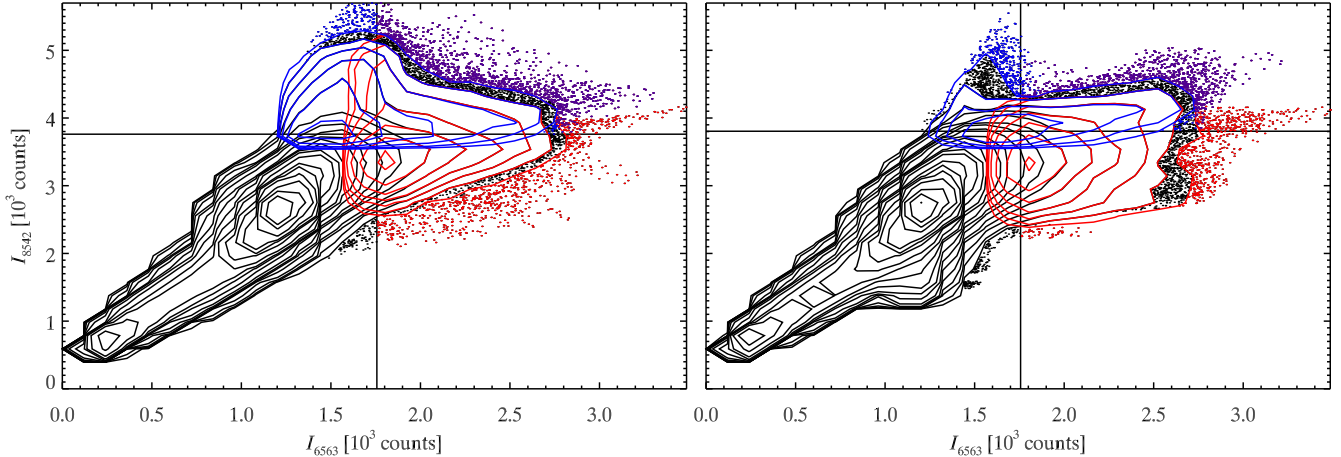


FIG. 4.— Scatter diagrams for $H\alpha$ versus Ca II 8542 Å blue wing (*left panel*) and red wing (*right panel*) for data set 1, with contours and points for all pixels (*black*), $H\alpha$ detection pixels (*red*) and Ca II detection pixels (*blue*). Sample density contours are plotted where high sample numbers occur to avoid plot saturation. Pixels outside the contours that are common to both $H\alpha$ and Ca II detections are correspondingly purple. The vertical and horizontal lines specify the 140% thresholds of the average intensity over the field of view for $H\alpha$ and Ca II, respectively.

quite variable in both shape and intensity in their temporal evolution. Note that not all $H\alpha$ detections have a corresponding detection in Ca II (e.g., the azure contour in the upper right of the lower eight panels). Although the shapes of the detection contours based on the $H\alpha$ and Ca II images, respectively, often overlap, this overlap is typically not one-to-one (cf. the differences between the detection contours in the upper four rows). Also, the detections in the blue and red wings of Ca II are usually quite dissimilar, as shown by the corresponding blue and red contours in the upper rows of Fig. 3.

Figure 4 quantifies these observations in the form of scatter diagrams. For the majority of pixels in this data set, and in particular for those with an intensity below a 140% of average cutoff in either diagnostic (i.e., the lower left quadrant), there is a tight correlation between the $H\alpha$ and Ca II intensities. It continues to larger brightness values in both spectral lines regardless whether the blue or red wing of Ca II is considered, although clearest in the latter. Furthermore, above both thresholds (upper right quadrant) most bright pixels are detected as Ellerman bombs in both diagnostics, but some of the brighter $H\alpha$ -detected pixels above the Ca II threshold are not detected as such in either Ca II wing. Conversely, a considerable number of the brighter Ca II pixels falls below the $H\alpha$ threshold (i.e., the high Ca II-intensity peak near the $H\alpha$ threshold and in the upper left quadrant). Also, and in contrast to the blue wing of Ca II, there are relatively more pixels in the Ca II red wing that are bright in $H\alpha$ but no so much in Ca II, e.g., the “lump” in the black contours around $I_{6563} = 1200$ counts and the more extended contours above the $H\alpha$ and below the Ca II thresholds in the right-hand panel.

Figure 5 shows the detection-averaged profiles for Ellerman bombs observed in Ca II 8542 Å and $H\alpha$ along with the profile averaged over the full SST field-of-view for both lines. The upper and middle panel show the profiles in the summed blue and red wings of Ca II, respectively. Most profiles appear to peak around ± 0.5 – 0.6 Å from line center and are asymmetric in shape. The blue wing detections have a general tendency to be brighter in

the blue wing, while those in the red wing show the opposite effect, although the picture is much more confusing in the latter case. We also detect more Ellerman bombs for which the maximum brightness in the red wing is more than 10% larger than that in the blue wing (three of which have a red wing brightness that exceeds that of the blue wing by more than 20%), than we do with the opposite asymmetry. The lower panel of the same figure shows the detection-averaged profiles for Ellerman bombs in $H\alpha$ in the first data set. Only 16 out of 78 profiles show some sort of asymmetry, although less strongly than for the Ca II detections (i.e., all asymmetric profiles have the brightest wing exceeding the less bright wing by no more than 10%). The majority of those asymmetric profiles have a blue-brighter-than-red wing signature.

Signature in AIA 1700 Å— As already pointed out in the introduction, images taken in the 1700 Å continuum reproduce a similar patchwork of bright network as observed in Ca II 8542 Å with localized brightenings that seem to correspond closely to Ellerman bombs (cf. Figs. 1 and 2). Figure 6 shows this in more detail by displaying part of the time evolution of region-of-interest 2 in $H\alpha$ and several AIA channels, with $H\alpha$ and 1700 Å detection contours overlaid (here we focus on the first two columns and postpone discussion of the remaining panels to the end of this section). Comparison of the $H\alpha$ and 1700 Å intensity images, as well as the detection contours on both, shows that co-temporal brightenings can be found in 1700 Å, albeit at lower spatial resolution than in the $H\alpha$ data and, consequently, with differing morphology and extent. However, a $5\text{-}\sigma$ above average threshold does a relatively good job in recovering the brighter Ellerman bombs as well as Ellerman bomb conglomerates.

For a more detailed comparison we degraded our CRISP $H\alpha$ data to the much coarser pixel size of the AIA 1700 Å data, i.e., $0''.6 \text{ px}^{-1}$. Figure 7 shows scatter diagrams of these data, where the red contours and points are based on the $H\alpha$ detections in the higher resolution CRISP data. A further limiting criterion is that of the pixels exceeding $5\text{-}\sigma$ above average intensity in

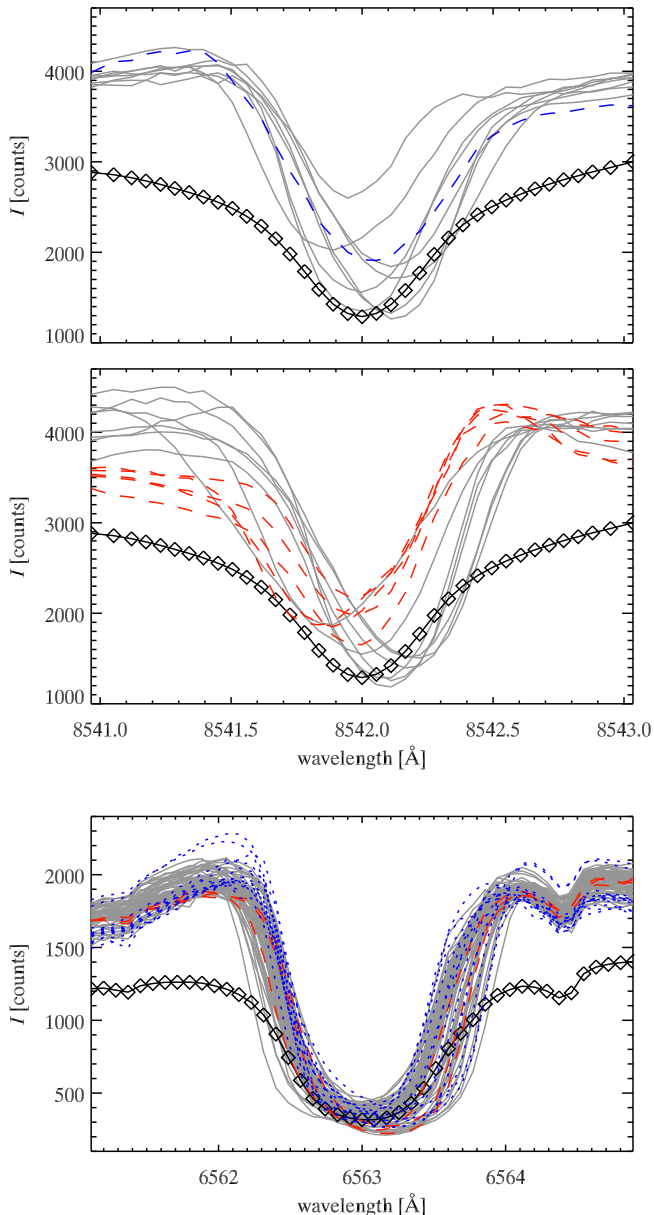


FIG. 5.— Profiles for Ellerman bomb detections in the Ca II 8542 Å blue wing (*upper panel*), red wing (*middle panel*) and in H α (*lower panel*). Upper two panels: profiles of detections with blue-brighter-than-red (*dashed blue*) or red-brighter-than-blue (*dashed red*) asymmetry by least 10% and all other detections (*solid grey*). Lower panel: profiles of detections with at least 5% blue-brighter-than-red asymmetry (*dotted blue*), red-brighter-than-blue asymmetry (*dashed red*) and all other detections (*solid grey*). In all panels the field-of-view average profile is also indicated (*solid black with diamonds*).

1700 Å, only those that persist at such intensity for a period shorter than 5 minutes were included. Note that the number of pixels at SST resolution was retained in downsampling the H α data and that the 1700 Å were up-scaled to the same number of pixels as the SST data (but retaining the same SDO-sized pixel-shapes, e.g., Fig. 6). The apparent quantization effect in the scatter clouds outside the contours is caused by both that and by the fact that within the considered fields-of-view and time spans the high-intensity values are not continuous.

We find a large degree of correlation for both data sets by excluding pixels with H α brightness of less than about 1000 counts, although not as tight as for the H α -Ca II comparison. The low-1700 Å/lower-H α intensity “tongue” in both panels corresponds to the sunspots and is more pronounced for data set 1 due to (1) the sunspot covering a larger portion of the field-of-view, and (2) the absence of the lower-H α /medium-1700 Å intensity bulge in the lower left quadrant of the scatter diagram for data set 1. The latter is probably a result of sampling brighter network at 1700 Å while strong absorptions are present at those pixels in the summed wings of H α for the second data set.

Considering only the pixels based on high-resolution H α detections (red contours and points) we find that part of the Ellerman bombs would be recovered also in the lower resolution H α data (even more so in the second than in the first data set), but would have too low 1700 Å brightness to distinguish them from regular network in those data. That the bulge of detection pixels falls below the H α threshold (i.e., in the lower left quadrant) in both data sets is a result of downsampling the CRISP data. Interestingly though, many of the pixels above a 5- σ threshold in 1700 Å are the same pixels as recovered by the H α detections and if increased to 8- σ (corresponding to roughly 3100 and 8500 counts for data sets 1 and 2, respectively) the overlap would be near-perfect with respect to the brightest H α Ellerman bombs. Also, when applying the detection algorithm to the lower resolution H α data, we recover 19 and 23 detections (corresponding to about 24% and 38% of the detections in the high-resolution H α data) in the first and second data set, respectively, comparable to the 1700 Å detection numbers.

Occurrence location and magnetic field— Figure 8 shows the time sequence of a few Ellerman bombs in regions-of-interest 2 and 3. Comparison of the H α and Fe I 6301 Å Stokes-V/I images shows that Ellerman bombs can generally be observed at locations where opposite polarities meet, i.e., the Ellerman bombs occur on the inversion line between the opposite polarities and sometimes appear rooted in patches of both positive and negative polarity. Several examples of these properties are given in Figs. 8 and 9 for regions-of-interest 2 through 5. In particular, the Ellerman bomb in the top three rows and the larger Ellerman bomb cluster in the following three rows of Fig. 8 exhibit the rooting in opposite polarities, but it suggests itself also for some of the Ellerman bombs in the lower panels of the two regions-of-interest in Fig. 9. Quantitatively, this observation translates into Fig. 10, showing histograms of the separation between opposite polarities for all pixels (solid line) and detection pixels only (dashed line). While the distribution of the opposite polarity separation for all pixels (i.e., also including Ellerman bomb detections), peaks in the 1''0–1''5 bin and has an average of 5''7, that of the Ellerman bomb detection pixels alone is much narrower, peaking in the first bin and averaging at 0''9.

In a small number of cases, an opposite polarity cannot be observed in the vicinity of the Ellerman bomb, an example of which is given in right-hand columns of Fig. 8. The Ellerman bomb in this figure seems to be rooted exclusively in a positive polarity patch with no sign of any

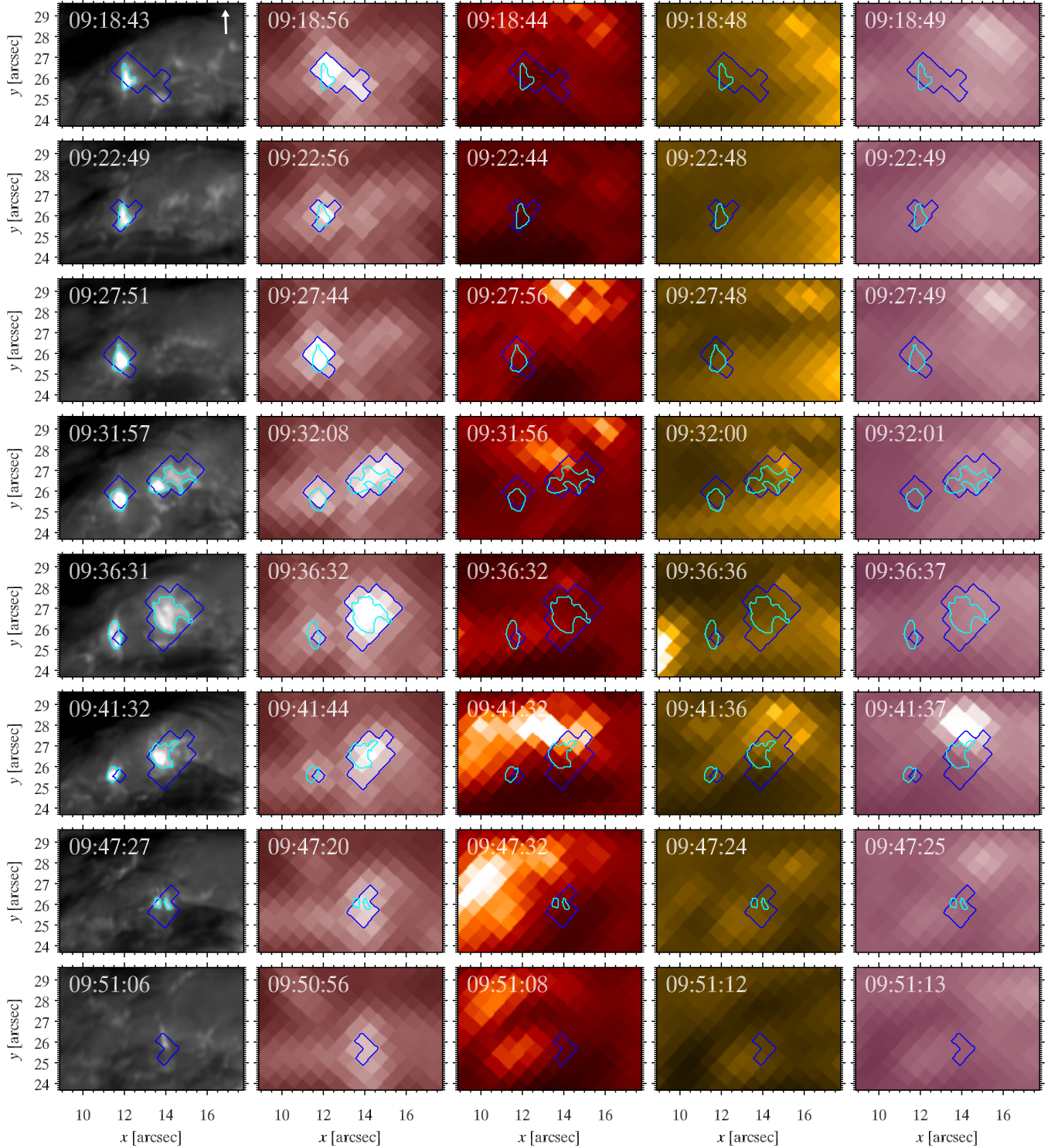


FIG. 6.— Time evolution of a sequence of cutouts corresponding to region-of-interest 2. From left to right: CRISP images in the summed wings of H α , AIA images in the continuum at 1700 \AA , He II 304 \AA , Fe IX 171 \AA , and Fe XIV 211 \AA . The cutouts are rotated counter-clockwise by 48 $^\circ$ from their orientation in Fig. 2 to obtain a near-vertical limbward direction, indicated by the white arrow in the top left panel. The contours specify results of the detection algorithm applied to H α (azure) and 1700 \AA (dark blue). The time in UT is given in the upper left corner of the first column panels.

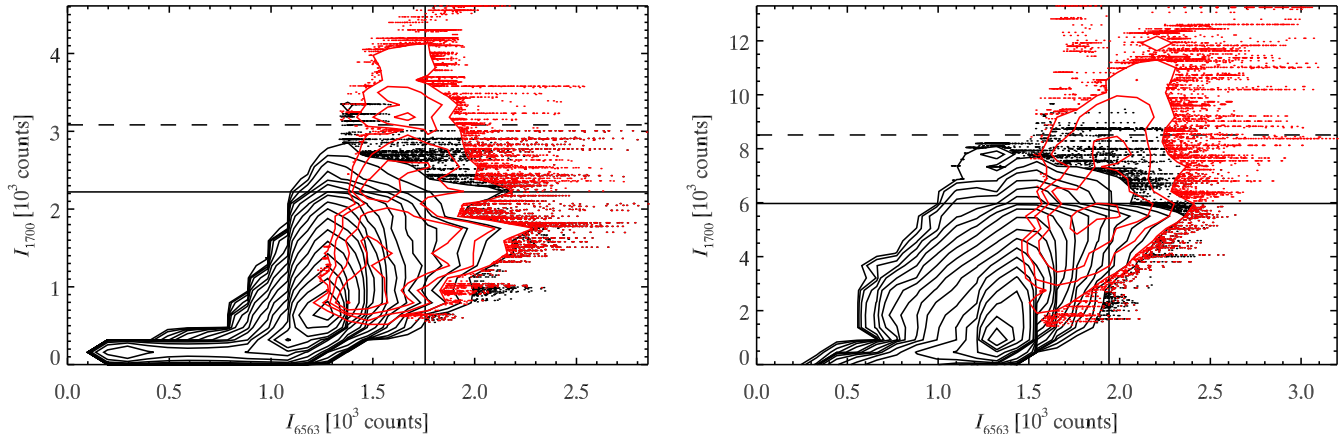


FIG. 7.— CRISP $H\alpha$ versus AIA 1700 Å scatter diagrams for data set 1 (left panel) and data set 2 (right panel). As in Fig. 4, contours and points are drawn for all pixels (black) and $H\alpha$ detection pixels only (red). The vertical solid line specifies the 140% of average intensity threshold for $H\alpha$. The horizontal lines specify the 5- σ (solid) and 8- σ (dashed) above average intensity for 1700 Å.

opposite polarity patch during (or prior to) its lifetime. It is also notably smaller and less bright than the Ellerman bombs in regions-of-interest 2, 4 and 5, which appears to be generally the case for Ellerman bombs in a (seemingly) unipolar magnetic field configuration.

Comparing the occurrence locations of Ellerman bombs to the surface flow field arrows in Figs. 8 and 9 the Ellerman bombs seem to appear where the magnetic field has been or is being pushed around. Examples of this are numerous in said figures, e.g., the flow field arrows (1) above and behind the Ellerman bomb in the top three rows of the left-hand columns in Fig. 8, (2) prior to and during the large Ellerman bomb cluster in the same region-of-interest, starting at 09:31:57, (3) nearby the Ellerman bomb location in the first, third, sixth and seventh panels of the right-hand columns in the same figure (although the flow field strength is noticeably smaller than in other examples), (4) above the negative polarity patch prior to the Ellerman bomb in the left-hand columns of Fig. 9, (5) in the vicinity of the opposite polarity patches in the right-hand part of the right-hand columns, both prior to and during the presence of an elongated Ellerman bomb in the lower two rows, (6) above the faint negative polarity patch (blue) prior to the Ellerman bomb on the right-hand side of the same region-of-interest. Both the first and fifth are telltale examples of opposite polarities being pushed towards (and in the latter case also alongside) each other, as the negative polarity patches move from $(x, y) \approx (12.5, 26.0)$ to $(x, y) \approx (11.8, 25.5)$ in Fig. 8 and from $(x, y) \approx (37.5, 38.0)$ to $(x, y) \approx (37.0, 37.0)$ (towards and alongside a near-stationary positive polarity) in Fig. 9. Moreover, the size and strength of the opposite polarity patches in the bipolar configurations are greatly reduced during the Ellerman bomb lifetimes and in some cases one of the polarities even vanishes completely. Most notable examples of this are the first, second, fifth and sixth in the list above.

Comparison with outer atmosphere diagnostics— Considering that earlier studies have reported Ellerman bomb-related surges, we investigated whether the upper atmospheric AIA data showed any signs of perturbation by the underlying Ellerman bombs. Figure 6 shows the time evolution of the second region-of-interest as observed by

both CRISP (in the summed wings of $H\alpha$) and AIA (in the continuum at 1700 Å, He II 304 Å, Fe IX 171 Å, and Fe XIV 211 Å). This particular region-of-interest and time span (the same as Fig. 8) were chosen as it shows both the brightest Ellerman bombs of the field-of-view during the time series and presents the most tempting case for co-relating Ellerman bomb presence with activity in the higher atmosphere.

Comparison of the $H\alpha$ and He II 304 Å images generally shows no clear correspondence, even though sometimes the He II 304 Å images do display brightenings nearby, but not co-spatial with, the underlying Ellerman bombs observed in the $H\alpha$ wings (e.g., the fourth, sixth and seventh rows in Fig. 6). To a lesser extent this also holds for Fe IX 171 Å and Fe XIV 211 Å (cf. the sixth and seventh rows). However, when taking the bigger field-of-view shown in Fig. 2 into account, the aforementioned brightenings in He II 304 Å, Fe IX 171 Å, and Fe XIV 211 Å seem rather a result of inflows along larger scale structures and originate outside the field-of-view of the SST. Ellerman bombs elsewhere in the field-of-view do not result in any perceivable signal in these diagnostics either and running time-difference movies of the AIA data are equally inconclusive.

5. DISCUSSION

Visibility in $H\alpha$ — Ellerman bombs are traditionally defined as temporary brightenings of the outer $H\alpha$ wings in emerging flux regions that have no signature in the $H\alpha$ core (Ellerman 1917). However, the fourth and fifth panels of Fig. 1 show many $H\alpha$ -wing bright points near the spot that are not Ellerman bombs but mark more ubiquitous and stable kilogauss magnetic concentrations, similarly to G-band bright points (Leenaarts et al. 2006a; 2006b). They are a subset of the magnetic bright points in the first three panels of Fig. 1 where the first shows them the sharpest but with the lowest contrast (best with enlargement in a pdf viewer). The second panel shows them less sharp, due to higher-up radiation escape and scattering. The third panel renders them very similar to the second, except for the large difference in telescope resolution. The $H\alpha$ wing panels in the second row show only those that are not shielded by overlying

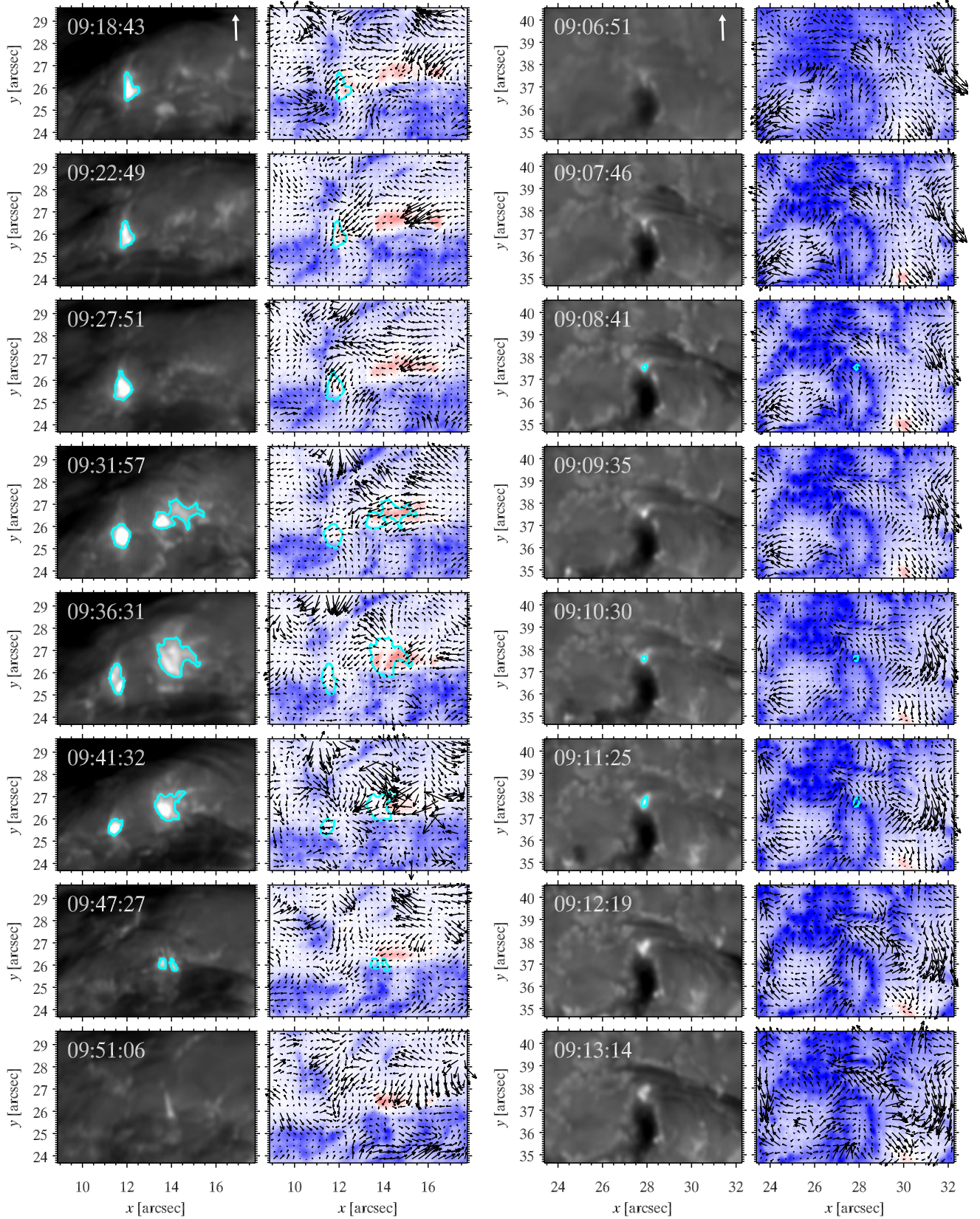


FIG. 8.— Ellerman bomb evolution (azure contours) in region-of-interest 2 (*left-hand columns*) and region-of-interest 3 (*right-hand columns*). *First column*: H α summed wings images for region-of-interest 2. *Second column*: Fe 16301 \AA Stokes-V/I images for the same region of interest, with positive/negative values shown in red/blue and small black arrows indicating the surface flow field (we suggest zoom-in with a pdf viewer). *Third column*: H α summed wings images for region-of-interest 3. *Fourth column*: Fe 16301 \AA Stokes-V/I images for the same region of interest (format as for the second column panels). The Stokes-V/I panels have been scaled to the full SST field-of-view at the first time step to enable comparison between the different regions-of-interest. The H α panels have been scaled independently for each region-of-interest. The arrows in the top panel of the first and third columns indicate the limbward direction. The time in UT is given in the upper left corner of the first and third column panels.

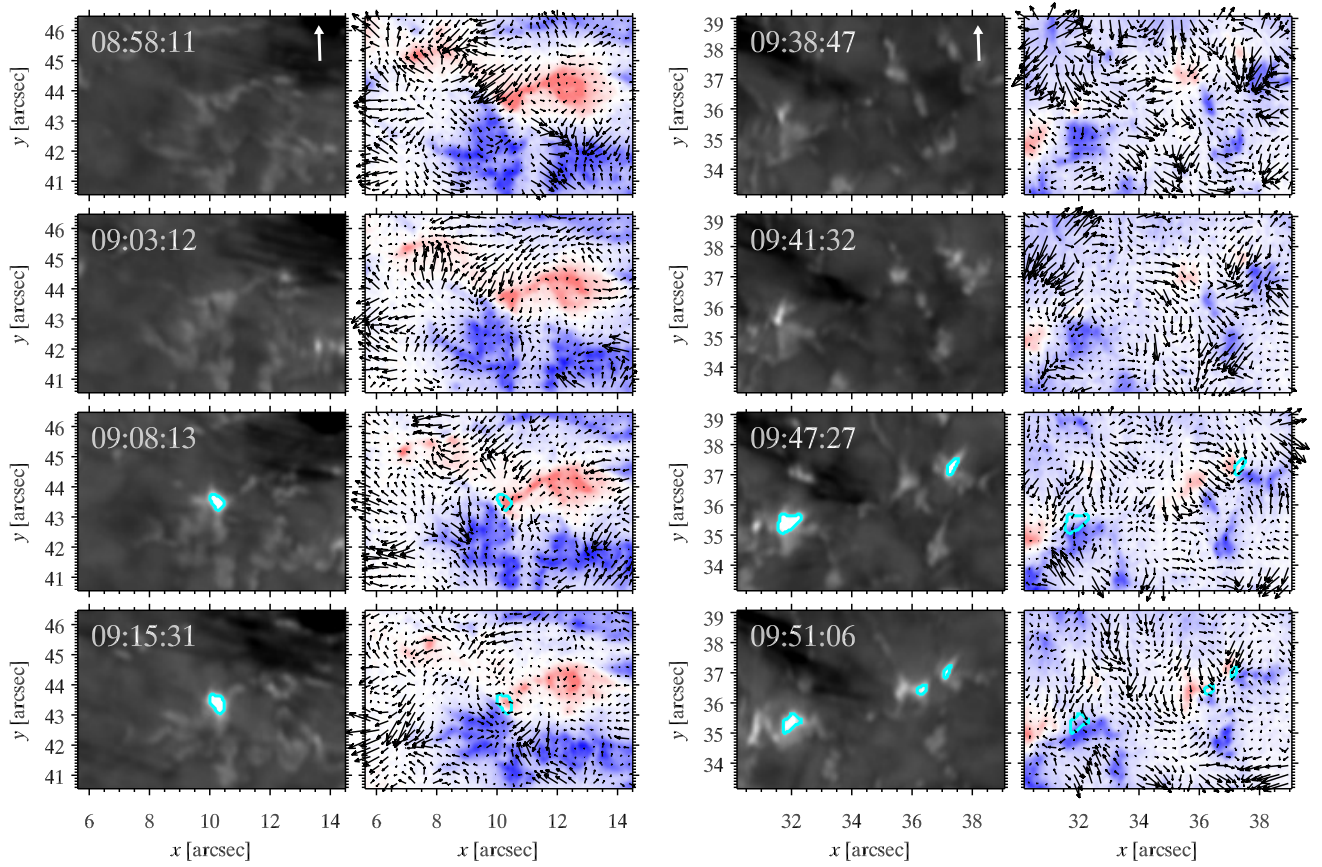


FIG. 9.— Ellerman bomb evolution in two more regions of interest marked in Fig. 2: region-of-interest 4 (*left-hand columns*) and region-of-interest 5 (*right-hand columns*). Further format as for Fig. 8.

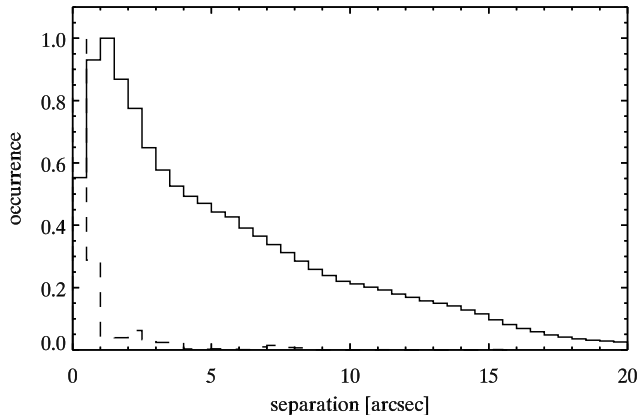


FIG. 10.— Distribution of the separation between opposite polarities for all pixels (*solid line*) and Ellerman bomb detection pixels (*dashed line*) in the field of view of data set 2, excluding the sunspot, for frames with above average contrast. Both distributions have a bin size $0''.5$ and have been scaled to their respective maximum values.

fibrils, with slight defocus caused by scattering in the transparent fibrils. Such “pseudo Ellerman bombs” are discussed in more detail in Rutten et al. (2013). Figures 3, 8, and 9 demonstrate, as did Paper I, that at the superb SST resolution in slanted limbward viewing, proper Ellerman bombs show up as yet brighter, upright, short-lived, rapidly varying, elongated flames. We now prefer to define Ellerman bombs observationally as $H\alpha$ -wing features with this flame morphology. Our detection algorithm is tailored to identify those features that we recognized visually as such flames.

Detection— In this study, we define a fully automated detection algorithm to select Ellerman bombs in both $H\alpha$ and $Ca\ II\ 8542\ \text{\AA}$ wing data. This is a different approach from Paper I, where only the network bright points were detected automatically and Ellerman bombs selected manually afterwards. The detection constraints listed in Sect. 3.1 (kernel brightness $>155\%$ of average, adjacent brightness $>140\%$ of average, minimum size of $0''.2$ – $0''.3$, minimum lifetime of ~ 50 s) are therefore different in several respects from those presented in Paper I, although most notably with respect to the minimum lifetime (240 s in Paper I). However, visual inspection of the results suggests that these constraints are adequate in selecting events that, in addition to excess wing brightness, display the telltale upright, flame-like morphology while excluding pseudo Ellerman bombs.

The number of Ellerman bombs we find in our data is modest compared to some earlier studies. For example, the birthrate of Zachariadis et al. (1987, $1.5\ \text{min}^{-1}$ in an $18''\times 24''$ region) would predict about 510 and 590 Ellerman bombs in our first and second data set, respectively. Even larger numbers were obtained in a recent study by Nelson et al. (2013) who reported on the automated detection of 3570 Ellerman bombs in a 90 minute time series of $96''\times 96''$ $H\alpha$ data obtained with the IBIS instrument. Their detection algorithm differs from ours mainly in its intensity threshold (130% of the average brightness), no minimum lifetime, and by considering events that fade below and brighten again to above the threshold as separate events (i.e., to account for seeing effects we allow up to ~ 50 s of non-detection for spatially overlapping events

to be considered the same). The only way of detecting more events in our case would be to relax the intensity thresholds. The 140% and 155% of the field-of-view averaged brightness thresholds for both $H\alpha$ and $Ca\ II$ that we used are much more restrictive than the threshold adopted by Nelson et al. (2013) or the Ellerman bomb contrast range of 105%–130% reported earlier by Georgoulis et al. (2002). Conserving all other constraints, tests with lower than 155% initial thresholds resulted in detection of many network bright points and features that, in our opinion, are not Ellerman bombs.

Most previous studies have reported Ellerman bomb lifetimes between 10–20 min, in some cases even up to 30 min (e.g., Qiu et al. 2000; Fang et al. 2006; Matsumoto et al. 2008a; Watanabe et al. 2008; Herlender & Berlicki 2011; Paper I). The average lifetime we find for Ellerman bomb detections, 3.5–4 min, is much shorter than that reported in Paper I, which can largely be attributed to a more relaxed minimum lifetime threshold (240 s in Paper I versus ~ 50 s here), although a few seem to last as long as the earlier reported 20–30 min. However, these longer detections typically display substructure and repetitive flaring and the lifetime of such substructure is much shorter than the ensemble lifetime. Similarly, the longer-lived detections in $1700\ \text{\AA}$ tend to coincide with multiple shorter-lived $H\alpha$ detections, which may explain the longer average lifetime for $1700\ \text{\AA}$ detections. Our present results are comparable to those obtained for Ellerman bombs by e.g., Pariat et al. (2007a, reporting lifetimes between 1.5–7 min with a peak around 3–4 min).

The elongated substructures in our observations are typically $1''$ tall and about $0''.2$ wide. However, with 0.2 – $0.3\ \text{arcsec}^2$, the average area of single $H\alpha$ detections is much smaller than the 1 – $2\ \text{arcsec}^2$ reported before (e.g., Georgoulis et al. 2002; Fang et al. 2006; Pariat et al. 2007a; Matsumoto et al. 2008b). The smaller sizes we find are most likely a result of the higher spatial resolution of the images, as single detections in AIA $1700\ \text{\AA}$ data, with a pixel size of $0''.6\ \text{px}^{-1}$, are similar in size to those reported earlier.

Visibility in other diagnostics— Qiu et al. (2000) and Georgoulis et al. (2002) found that only about half of the Ellerman bombs identified in $H\alpha$ correspond to brightenings in TRACE $1600\ \text{\AA}$ images, while Berlicki et al. (2010) reported that all Ellerman bombs they found in $H\alpha$ images from the Dutch Open Telescope coincided with TRACE $1600\ \text{\AA}$ brightenings. Pariat et al. (2007a), comparing THEMIS $Ca\ II\ 8542\ \text{\AA}$ and TRACE $1600\ \text{\AA}$ data, also found a good correlation between the Ellerman bomb locations in both diagnostics.

From our data we find that only part of the Ellerman bombs in $H\alpha$ coincide with brightenings in $1600\ \text{\AA}$ and $1700\ \text{\AA}$, in agreement with Qiu et al. (2000) and Georgoulis et al. (2002). Although $1600\ \text{\AA}$ offers greater intensity contrast for the Ellerman bombs than $1700\ \text{\AA}$, it suffers noticeably from transition region contamination through the $C\ IV$ lines, complicating the application of an automated detection algorithm and thereby rendering $1700\ \text{\AA}$ the better AIA diagnostic for Ellerman bomb detection. Necessarily, only the larger and brighter Ellerman bombs or the enveloping haloes of multiple

smaller Ellerman bombs are observable in the 1700 Å data (cf. Figs. 1, 2, and 6), given that their spatial resolution is lower than that of the CRISP data. This is further supported by the detection numbers and statistical evidence in Fig. 7, showing that most of the H α detected Ellerman bombs cover pixels that in 1700 Å have an intensity that cannot be differentiated from that of regular network and only the brighter H α pixels exceed the 5- σ threshold in 1700 Å (more so for the second than for the first data set). Notwithstanding, our results suggest that modifying the detection algorithm from Sect. 3.1 to incorporate a brightness threshold of 8- σ above average, as well as an upper limit of 5 minutes on the lifetime would provide an effective recipe to detect Ellerman bombs in 1700 Å, possibly expanded with a maximum size to prevent detection of flare-like events. Even though not all Ellerman bombs visible in the CRISP H α data would be recovered this way, AIA 1700 Å has the clear advantage of providing near-continuous imaging of the entire Earth-side solar disk.

Comparing the detections in H α and Ca II 8542 Å shows that only part of the detections in the former have a good spatial overlap with those in the Ca II blue and red wing. Such discrepancy in morphology between Ellerman bombs in these two lines has not been reported before. For most Ellerman bombs we find a clear morphological dissimilarity (cf. Figs. 3 and 4). This is the case both when comparing H α with either wing of Ca II, as well as the wings of the latter with each other. As illustrated in Fig. 3, in some cases the brightenings in Ca II lag behind those in H α (with respect to the proper motion of the Ellerman bombs) or appear on top of those. We speculate this may be due to projection effects, as we find that the well-overlapping detections concern Ellerman bombs that have a proper motion roughly along the line-of-sight, whereas those that overlap only partly detect Ellerman bombs moving at an angle to the line-of-sight. Additional effects explaining the spatial differences could be the difference in recombination rate and opacity between the two lines. Both H α and Ca II 8542 Å probably show the afterglow of subsequent recombination (Rutten et al. 2013), while the reconnection likely takes place on very small spatial and temporal scales. Different recombination rates and Ca II having opacity surrounding the Ellerman bomb where H α has none, may cause significant differences in the morphology of Ellerman bombs as observed in both lines.

Some of the Ellerman bombs detected in the Ca II blue wing are not detected in the red wing, and vice versa, which may be explained by an asymmetry in their respective spectral profiles. Such asymmetry has been known for a long time from Ellerman bomb studies in H α (e.g., Severny 1968; Engvold & Maltby 1968; Koval & Severny 1970; Bruzek 1972; Kitai 1983), Ca II 8542 Å (e.g., Fang et al. 2006; Socas-Navarro et al. 2006), and Ca II H (Hashimoto et al. 2010). The blue-asymmetry (i.e., the blue wing brighter than the red wing) is the most common, but opposite asymmetries (or lack of a strong trend) have also been reported (Fang et al. 2006; Socas-Navarro et al. 2006; Pariat et al. 2007a), as well as asymmetry changes within Ellerman bombs during their lifetimes (Hashimoto et al. 2010).

We find no strong evidence of such asymmetry in

the detection-averaged H α profiles of data set 1. Only about 20% of the profiles have an appreciable wing-excess asymmetry (the majority of those are blue-asymmetric, in accordance with previous reports), but none have the intensity in one wing exceeding that in the other by more than 10%. However, in contrast to the findings of Fang et al. (2006) and Pariat et al. (2007a), the Ellerman bombs in our Ca II images appear to suffer more from these asymmetries, being both more prevalent and stronger (cf. the top panels of Fig. 5). It should be noted that the Ca II 8542 Å wing images we present in this work have been obtained by summing over a small range around ± 0.6 Å from Ca II line center, which is further out than the ± 0.35 Å where Pariat et al. (2007a) reported intensity peaks in the Ca II spectrum (while the spectral passband is comparable). Although some of the Ca II brightenings we observe in the blue and red wings appear to be visible closer to line center as well, the view at ± 0.35 Å is permeated with fibrillar structures comparable to H α ± 0.5 Å (panels 5 and 6 in Fig. 2), complicating the clear identification of Ellerman bombs (Paper I; Rutten et al. 2013).

The profile asymmetry is well explained as a result of overlying, Doppershifted fibrils (as pointed out in Bruzek 1972, Kitai 1983, Dara et al. 1997, Paper I, and Rutten et al. 2013). The superpenumbral fibrils on the disk-center side of the sunspot show a stronger absorption in the red wing, while those on the limb-side are darker in the blue wing, i.e., the line core is shifted blue-wards on the limb-side and red-wards on the disk-center side (signature of the inverse Evershed flow along those fibrils, Evershed 1909). The fifth and sixth panels of Fig. 1 illustrate this clearly. As the atomic mass of calcium is larger than that of hydrogen, the thermal width of Ca II 8542 Å is much smaller and its sensitivity to this effect is consequently larger. The asymmetries that result by the overlying Dopplershifted fibrils eating up the emission signal is thus more pronounced in Ca II and may also explain why less Ellerman bombs were detected in Ca II.

Full explanation of the different appearance of Ellerman bombs in different diagnostics requires detailed radiative transfer modeling while such morphological differences may well provide important constraints to numerical Ellerman bomb simulation in the first place. However, such studies are beyond the scope of this paper. Some of the line formation suggestions of Rutten et al. (2013) are presently being tested by the Oslo group.

Triggering—Magnetic reconnection has been proposed in many previous studies as the driving mechanism of Ellerman bombs, although the actual field topology is still debated (e.g., Georgoulis et al. 2002; Pariat et al. 2004; Watanabe et al. 2008; Matsumoto et al. 2008b; Hashimoto et al. 2010; Pariat et al. 2012b). Evidence for bidirectional flows in Ellerman bombs has been found in Ca II H (Matsumoto et al. 2008a) and H α data (Paper I). Combined with the jet-like structure reported here and in Paper I, this could be indicative of reconnection by a mechanism similar to that in so-called anemone jets (Shibata et al. 2007; Morita et al. 2010; Nishizuka et al. 2011). The majority of the Ellerman bombs are found along magnetic polarity inversion lines (e.g., Fang

et al. 2006; Pariat et al. 2007a; Matsumoto et al. 2008b; Hashimoto et al. 2010), but an appreciable fraction is observed in apparently unipolar configurations (Qiu et al. 2000; Georgoulis et al. 2002; Watanabe et al. 2008).

We find that most Ellerman bombs in the field-of-view of the second data set occur where opposite polarities meet, although not all locations with adjacent bipolar fields result in an Ellerman bomb. In agreement with Hashimoto et al. (2010), we observe that one or both of the polarity patches decreases in strength during the Ellerman bomb lifetime. Typically the smaller patch also shrinks, sometimes to the point that it completely disappears, but this could be a detection sensitivity effect of our Fe 16301 Å Stokes- V/I data. In addition, our simultaneous photospheric surface flow maps show that patches of opposite polarity are in many events driven towards each other, either head-on or in a shearing motion. This is consistent with a configuration similar to that in cartoon 1 in Fig. 17 of Watanabe et al. 2008 or Fig. 19 in Hashimoto et al. (2010), although it does not rule out a scenario in which flux emerges resistively and reconnects with existing fields (e.g., Isobe et al. 2007; Pariat et al. 2012b). The surface flows are typically strongest just prior to the detection of the Ellerman bombs with the Ellerman bombs moving in the direction of the flows. The latter was already described in Paper I, but here we provide further quantitative evidence.

However, not all Ellerman bomb detections correspond to locations with clear opposite polarity patches and we find a number of them in apparently unipolar regions, close to the sunspot penumbra (e.g., the event in the third and fourth columns of Fig. 8). This could be indicative of unipolar shearing reconnection (e.g., Watanabe et al. 2008) or, alternatively, the opposite polarity is too weak to be detected. The latter is a realistic possibility, considering the typically smaller size and lower brightness of unipolar events, as well as that they tend to occur close to the penumbra, where the field is stronger.

Effect on the upper atmosphere— As noted in the introduction, correspondence of Ellerman bombs with surges and high-energy events in the upper atmosphere has been reported but seems not ubiquitous (Schmieder et al. 2004). In Paper I only 2 out of 17 Ellerman bombs presented a possibly related surge; here we found none. In our comparison of the high-cadence upper atmospheric AIA data in He II 304 Å, Fe IX 171 Å, and Fe XIV 211 Å with the Ellerman bomb locations in $H\alpha$ we find no conclusive evidence for co-related upper atmosphere signals. The most tempting case was found in data set 2, where multiple Ellerman bombs are occurring while co-temporal and nearly co-spatial brightenings are observed in He II 304 Å and Fe XIV 211 Å, and to some extent in Fe IX 171 Å (cf. Fig. 6). Although these brightenings could be linked to the underlying Ellerman bombs, the dynamics in the larger field-of-view suggest they are rather related to flows along the larger loop-like structures that extend to beyond the field-of-view of the SST. Also, equally bright Ellerman bombs elsewhere in the field-of-view produce no perceivable effects in either 304 Å, 171 Å or 211 Å. Similarly, $H\alpha$ and Ca II 8542 Å images closer to line center, i.e., sampling greater heights

than the far wings, show no evidence for Ellerman bomb-related surges. Hence, our data offer no support for the earlier claimed connections of Ellerman bombs to microflares, flaring arch filaments, or surges.

6. CONCLUSIONS

In this paper we have studied two active regions using high-resolution CRISP imaging spectroscopy in $H\alpha$ and Ca II 8542 Å, imaging spectropolarimetry in Fe 16301 Å, and AIA imaging in the UV-continua at 1600 Å and 1700 Å, in He II 304 Å, Fe IX 171 Å, and Fe XIV 211 Å. The co-spatial and co-temporal Fe 16301 Å Stokes- V/I data have allowed us to expand on the work previously presented in Paper I, by considering the relation of Ellerman bombs to the underlying magnetic field in more depth. On the other hand, simultaneous Ca II 8542 Å and AIA 1700 Å imaging has provided a multi-diagnostic view of Ellerman bombs, while the AIA 304 Å, 171 Å, and 211 Å data have enabled us to study possible Ellerman bomb effects on the upper atmosphere.

We find that a clear majority of the Ellerman bombs occurs where positive and negative polarities are driven together by the photospheric surface flows, enabling opposite polarity cancelation. A small number is also found in unipolar regions where shearing reconnection may take place. In either case, these results strengthen the case for a scenario in which frozen-in fields are carried by the moat flow around sunspots, causing Ellerman bombs as they reconnect. Morphologically, Ellerman bombs often appear dissimilar in Ca II 8542 Å and $H\alpha$, and we detect far fewer Ellerman bombs in Ca II than in $H\alpha$. Both may be due to the larger sensitivity of Ca II to Dopplershifts of the superpenumbral fibrils overhead, consequently producing the strong asymmetric Ellerman bomb profiles. The brighter Ellerman bombs also have distinguishing signature in AIA 1700 Å, although none of the finer substructure is observed in the lower resolution AIA images. However, even though automated detections in AIA 1700 Å would miss out on two thirds to three quarters of the Ellerman bombs visible in the $H\alpha$ wings, it may offer a straightforward way to track flux emergence in large active regions or even full-disk images, as well as enable the build-up of long-term, full-disk Ellerman bomb-statistics. Finally, no convincing evidence is found for influence from underlying Ellerman bombs on the outer atmosphere and we therefore conclude that Ellerman bombs are purely photospheric phenomena, incapable of breaking through the overlying canopy.

We thank Jaime de la Cruz Rodríguez and Eamon Scullion for their help during the observations. We also thank Eamon Scullion for providing the procedures for and helping with the co-alignment of the SDO/AIA and SST/CRISP data. We made much use of NASA's Astrophysics Data System Bibliographic Services. The Swedish 1-m Solar Telescope is operated on the island of La Palma by the Institute for Solar Physics of Stockholm University in the Spanish Observatorio del Roque de los Muchachos of the Instituto de Astrofísica de Canarias.

REFERENCES

- Archontis, V., & Hood, A. W. 2009, *A&A*, 508, 1469
- Berlicki, A., Heinzel, P., & Avrett, E. H. 2010, *Mem. Soc. Astron. Italiana*, 81, 646
- Bernasconi, P. N., Rust, D. M., Georgoulis, M. K., & Labonte, B. J. 2002, *Sol. Phys.*, 209, 119
- Bruzek, A. 1972, *Sol. Phys.*, 26, 94
- Cheung, M. C. M., Schüssler, M., Tarbell, T. D., & Title, A. M. 2008, *ApJ*, 687, 1373
- Dara, H. C., Alissandrakis, C. E., Zachariadis, T. G., & Georgakilas, A. A. 1997, *A&A*, 322, 653
- de la Cruz Rodríguez, J. 2012, PhD thesis, PhD Thesis, 2012
- Ellerman, F. 1917, *ApJ*, 46, 298
- Engvold, O., & Maltby, P. 1968, in *Mass Motions in Solar Flares and Related Phenomena*, ed. Y. Oehman, 109
- Evershed, J. 1909, *The Observatory*, 32, 291
- Fang, C., Tang, Y. H., Xu, Z., Ding, M. D., & Chen, P. F. 2006, *ApJ*, 643, 1325
- Georgoulis, M. K., Rust, D. M., Bernasconi, P. N., & Schmieder, B. 2002, *ApJ*, 575, 506
- Guglielmino, S. L., Bellot Rubio, L. R., Zuccarello, F., et al. 2010, *ApJ*, 724, 1083
- Hashimoto, Y., Kitai, R., Ichimoto, K., et al. 2010, *PASJ*, 62, 879
- Henriques, V. M. J. 2012, *A&A*, 548, A114
- Herlender, M., & Berlicki, A. 2011, *Central European Astrophysical Bulletin*, 35, 181
- Isobe, H., Tripathi, D., & Archontis, V. 2007, *ApJ*, 657, L53
- Kitai, R. 1983, *Sol. Phys.*, 87, 135
- Koval, A. N., & Severny, A. B. 1970, *Sol. Phys.*, 11, 276
- Leenaarts, J., Rutten, R. J., Carlsson, M., & Uitenbroek, H. 2006a, *A&A*, 452, L15
- Leenaarts, J., Rutten, R. J., Sütterlin, P., Carlsson, M., & Uitenbroek, H. 2006b, *A&A*, 449, 1209
- Lemen, J. R., Title, A. M., Akin, D. J., et al. 2012, *Sol. Phys.*, 275, 17
- Lites, B. W. 1987, *Appl. Opt.*, 26, 3838
- Litvinenko, Y. E. 1999, *ApJ*, 515, 435
- Madjarska, M. S., Doyle, J. G., & De Pontieu, B. 2009, *ApJ*, 701, 253
- Matsumoto, T., Kitai, R., Shibata, K., et al. 2008a, *PASJ*, 60, 95
- , 2008b, *PASJ*, 60, 577
- Morita, S., Shibata, K., Ueno, S., et al. 2010, *PASJ*, 62, 901
- Nelson, C. J., Doyle, J. G., Erdélyi, R., et al. 2013, *Sol. Phys.*, 283, 307
- Nishizuka, N., Nakamura, T., Kawate, T., Singh, K. A. P., & Shibata, K. 2011, *ApJ*, 731, 43
- Nozawa, S., Shibata, K., Matsumoto, R., et al. 1992, *ApJS*, 78, 267
- Pariat, E., Aulanier, G., Schmieder, B., et al. 2004, *ApJ*, 614, 1099
- , 2006, *Advances in Space Research*, 38, 902
- Pariat, E., Masson, S., & Aulanier, G. 2012a, in *Astronomical Society of the Pacific Conference Series*, Vol. 455, 4th Hinode Science Meeting: Unsolved Problems and Recent Insights, ed. L. Bellot Rubio, F. Reale, & M. Carlsson, 177
- Pariat, E., Schmieder, B., Berlicki, A., et al. 2007a, *A&A*, 473, 279
- Pariat, E., Schmieder, B., Berlicki, A., & López Ariste, A. 2007b, in *Astronomical Society of the Pacific Conference Series*, Vol. 368, *The Physics of Chromospheric Plasmas*, ed. P. Heinzel, I. Dorotović, & R. J. Rutten, 253
- Pariat, E., Schmieder, B., Masson, S., & Aulanier, G. 2012b, in *EAS Publications Series*, Vol. 55, *EAS Publications Series*, ed. M. Faurobert, C. Fang, & T. Corbard, 115–124
- Qiu, J., Ding, M. D., Wang, H., Denker, C., & Goode, P. R. 2000, *ApJ*, 544, L157
- Roy, J. R. 1973, *Sol. Phys.*, 28, 95
- Roy, J.-R., & Leparskas, H. 1973, *Sol. Phys.*, 30, 449
- Rutten, R. J., Vissers, G. J. M., Rouppe van der Voort, L. H. M., Sütterlin, P., & Vitas, N. 2013, *Journal of Physics Conference Series*, 440, 012007
- Scharmer, G. B., Bjelksjo, K., Korhonen, T. K., Lindberg, B., & Petterson, B. 2003a, in *Society of Photo-Optical Instrumentation Engineers (SPIE) Conference Series*, Vol. 4853, *Society of Photo-Optical Instrumentation Engineers (SPIE) Conference Series*, ed. S. L. Keil & S. V. Avakyan, 341–350
- Scharmer, G. B., Dettori, P. M., Löfdahl, M. G., & Shand, M. 2003b, in *Society of Photo-Optical Instrumentation Engineers (SPIE) Conference Series*, Vol. 4853, *Society of Photo-Optical Instrumentation Engineers (SPIE) Conference Series*, ed. S. L. Keil & S. V. Avakyan, 370–380
- Scharmer, G. B., Narayan, G., Hillberg, T., et al. 2008, *ApJ*, 689, L69
- Schmieder, B., Rust, D. M., Georgoulis, M. K., Démoulin, P., & Bernasconi, P. N. 2004, *ApJ*, 601, 530
- Schnerr, R. S., de La Cruz Rodríguez, J., & van Noort, M. 2011, *A&A*, 534, A45
- Severny, A. B. 1968, in *Mass Motions in Solar Flares and Related Phenomena*, ed. Y. Oehman, 71
- Shibata, K., Nishikawa, T., Kitai, R., & Suematsu, Y. 1982, *Sol. Phys.*, 77, 121
- Shibata, K., Nakamura, T., Matsumoto, T., et al. 2007, *Science*, 318, 1591
- Shimizu, T., Shine, R. A., Title, A. M., Tarbell, T. D., & Frank, Z. 2002, *ApJ*, 574, 1074
- Shine, R. A., Title, A. M., Tarbell, T. D., et al. 1994, *ApJ*, 430, 413
- Socas-Navarro, H., Martínez Pillet, V., Elmore, D., et al. 2006, *Sol. Phys.*, 235, 75
- van Noort, M., Rouppe van der Voort, L., & Löfdahl, M. G. 2005, *Sol. Phys.*, 228, 191
- Vissers, G., & Rouppe van der Voort, L. 2012, *ApJ*, 750, 22
- Watanabe, H., Bellot Rubio, L. R., de la Cruz Rodríguez, J., & Rouppe van der Voort, L. 2012, *ApJ*, 757, 49
- Watanabe, H., Vissers, G., Kitai, R., Rouppe van der Voort, L., & Rutten, R. J. 2011, *ApJ*, 736, 71
- Watanabe, H., Kitai, R., Okamoto, K., et al. 2008, *ApJ*, 684, 736
- Yi, Z., & Molowny-Horas, R. 1995, *A&A*, 295, 199
- Yokoyama, T., & Shibata, K. 1995, *Nature*, 375, 42
- Zachariadis, T. G., Alissandrakis, C. E., & Banos, G. 1987, *Sol. Phys.*, 108, 227